Microevents produced by gas migration and expulsion at the seabed: A study based on sea bottom recordings from the Sea of Marmara

J.-B. Tary, L. Geli, Claude Guennou, P Henry, Nabil Sultan, Namik Cagatay, Valérie Vidal

Microevents produced by gas migration and expulsion at the seabed: a study based on sea bottom recordings from the Sea of Marmara

J. B. Tary [1, *,] L. Géli [1], C. Guennou [2], P. Henry [3], N. Sultan [1], N. Çağatay [4], V. Vidal [5]

[1] Ifremer, Marine Geosciences Department, 29280 Plouzané, France
[2] UMR 6538, Oceanic Domains, University of Western Brittany, European Institute for Marine Studies (IUEM), 29280 Plouzané, France
[3] CEREGE, Aix-Marseille University, CNRS, UMR 6635, 13545 Aix-en-Provence Cedex 4,France
[4] Mining Faculty, Geology Department, Istanbul Technical University (ITU), Maslak, 34469 Istanbul, Turkey
[5] Université de Lyon, Laboratoire de Physique, École Normale Supérieure de Lyon, CNRS, 69364 Lyon cedex 07, France

*: Corresponding author : tary@ualberta.ca

Abstract:
Different types of 4-component ocean bottom seismometers (OBS) were deployed for variable durations ranging from 1 week to about 4 months in 2007, over soft sediments covering the seafloor of the Tekirdag Basin (western part of the Sea of Marmara, Turkey). Non-seismic microevents were recorded by the geophones, but generally not by the hydrophones, except when the hydrophone is located less than a few tens of centimetres above the seafloor. The microevents are characterized by short durations of less than 0.8 s, by frequencies ranging between 4 and 30 Hz, and by highly variable amplitudes. In addition, no correlation between OBSs was observed, except for two OBSs, located 10 m apart. Interestingly, a swarm of ~400 very similar microevents (based on principal component analysis) was recorded in less than one day by an OBS located in the close vicinity of an active, gas-prone fault cutting through the upper sedimentary layers. The presence of gas in superficial sediments, together with analogies with laboratory experiments, suggest that gas migration followed by the collapse of fluid-filled cavities or conduits could be the source of the observed microevents. This work shows that OBSs may provide valuable information to improve our understanding of natural degassing processes from the seafloor.

Keywords: Time series analysis; Gas and hydrate systems; Body waves; Interface waves; Seismic attenuation; Wave propagation

1. Introduction – general context

The Sea of Marmara is located on the North Anatolian Fault zone in NW Turkey, a major transform-plate boundary that has produced devastating historical earthquakes along its 1600 km length. After the 1999 Izmit and Düzce earthquakes, the next large (Mw > 7) earthquake is expected close to the heavily populated (>15 million inhabitants) Istanbul Area (Fig. 1). Hence, the Sea of Marmara has been extensively surveyed during the last decade.

Several marine expeditions found gas emissions sites and brackish water seeps, along or near the main active faults scarps in the Sea of Marmara [*Alpar*, 1999; *Halbach et al.*, 2004; *Armijo et al.*, 2005; *Zitter et al.*, 2008; *Géli et al.*, 2008]. Moreover, recent sediment profiler (chirp) and multibeam echosounder data acquired during the MARMESONET cruise of R/V Le Suroit [*Géli et al.*, 2010] show the widespread presence of gas in the upper sediments and water column [*Dupré et al.*, 2010; *Tary*, 2011]. Geochemical analysis indicates that the gas is mainly methane, and has two different origins: 1) in basins, gas is dominantly of bacterial origin, likely resulting from the decomposition of organic material in the Pleistocene sediments; 2) on the Western High and Central High (Fig. 1), gas is dominantly thermogenic, originating from the Eocene-Oligocene Thrace Basin source rocks [*Bourry et al.*, 2009].

These observations and the high geohazard potential of the area are such that the Sea of Marmara has been identified as an unique, natural laboratory to study the relationships between fluids and seismicity through the EC-funded ESONET Network of Excellence (**E**uropean **S**eafloor **O**bservatory **Net**work). In order to prepare the implementation of permanent multidisciplinary seafloor observatories, two preparatory experiments were conducted in 2007 and 2009-2010. Here, we report observations of non-seismic micro-events detected by Ocean Bottom Seismometers (OBS) and show that these events are probably

related to gas emissions from shallow sediment layers (<5 m). These findings may help to better understand degassing processes from the seafloor. In the perspective of future multi-disciplinary seafloor observatories, our results may also help establish a method to detect and characterize episodes of gas accumulation and release in shallow sediments.

Figure 1

2. Instrument characteristics and environmental settings

Between May 14 and August 30, 2007, two different experiments were carried out in the western part of the Sea of Marmara with eight, autonomous OBSs of 5 different types: OldOBS, MicrOBS, ARMSS, SPAN, NEEDLE. The instrument locations, technical characteristics and recording periods are summarized in Table 1. Specific details, useful for the present paper, are given hereafter:

- OldOBS (deployed at sites J, K, L and M) are large instruments (1.5 m in height, weighing 240 kg) from Ifremer, designed to be deployed offboard the operating vessel. The geophones (Geospace GS-11D, its response curve is given in Fig. S1) are contained in an outer, pressure-resistant case resting on the seafloor, while the hydrophone is fixed on the instrument frame, ~0.9 m above the seafloor (Fig. 2).
- MicrOBS (deployed at site J2) is also an Ifremer instrument, weighing less than 20 kg, packaged within a 13” glass sphere, which includes the electronics, the batteries and the geophones (Geospace GS-11D). The hydrophone is fixed on the instrument frame, ~0.3 m above the seafloor. Like OldOBSs, MicrOBSs are deployed offboard the operating vessel.

- ARMSS (from *CGGVeritas*) consists of a 0.9 m long cylinder lying horizontally on the seafloor, with a head containing both the geophones (Geospace LT-101) and the hydrophone. The three geophones are arranged in a Galperin configuration, i.e. set orthogonally and all tilted at 54.7° to the vertical axis. A vibrating system mounted around the instrument's head optimizes the coupling with the seafloor.
- SPAN (from *CGGVeritas*) is a ~1 m bullet shaped instrument, with geophones (SEND "Full Tilt") integrated in a titanium container three-fourth buried in the soil, or a little more due to the soft character of sediments. The data of this instrument were too noisy to be used for quantitative signals analysis.
- NEEDLE (from *CGGVeritas*) consists of a 4.5 m long pipe inserted in the sediments. After penetration, a self corroding system was activated, which divided the pipe into 2 mechanically decoupled sections, the sensors (three SEND "Full Tilt" geophones and a hydrophone) being at the end of the lower section (~3 m long).

Figure 2

Table 1

In order to test the different coupling devices, the 5 types of OBSs were all deployed for a maximum duration of 25 days, between May 14th to June 9th, 2007. While the Ifremer instruments (OldOBS and MicrOBS) were launched offboard R/V L'Atalante, the instruments provided by *CGGVeritas* (SPAN, ARMSS and NEEDLE) were installed *in-situ* using *Nautile*, the submersible of Ifremer. The second experiment involved only the 4 OldOBSs of Ifremer, which were re-deployed on June 9th, 2007, to record the local micro-seismicity from the Western Sea of Marmara [*Tary et al.*, 2011].

Based on laboratory results obtained in comparable pressure and temperature conditions, linear corrections were applied to the instruments internal clocks. For the first experiment, the drift of the internal clock was directly estimated for each instrument, based on GPS synchronization before deployment and after recovery, 25 days later. In addition, we took

advantage of GPS-dated seismic shots recorded by the OBSs on May 23 and 24, 2007, which ascertained that the drift of the internal clocks were nearly linear during the first experiment. These shots were also used to improve the accuracy of the instruments position. For the second experiment (June 9th – August 30th, 2007), the direct estimation of the drift was not possible, because the OldOBS recordings stopped before the instruments recovery. The drifts of the internal clocks during the 2nd experiment were thus corrected by simply applying the clock drifts that were obtained for the first experiment.

Conversion factors, from digital (counts) into physical (µm/s or Pa) units are unknown, except for the hydrophone of the MicrOBS and for the geophones of the OldOBSs. Hence, seismic shots have been used to calibrate the instruments sensors relatively to the MicrOBS hydrophone and to the OldOBS geophones, which were used as references. Conversion factors were derived assuming that the peak-to-peak amplitude of the first P-wave train in response to one given seismic shot, fired with the surface vessel directly above the OBSs (Fig. 1c), is the same for all OBSs (Fig. S2 and Table S1). Necessary information for proper sensor calibration was only available for Ifremer instruments. Therefore the instrumental response of the different sensors was not removed and the calibration is only an approximate one. The frequency response of Geospace GS-11D geophones (Fig. S1, OldOBS and MicrOBS) is almost flat in the frequency band of the micro-events (4-30 Hz). The inter-calibrated amplitudes given hereafter will be used to compare the different OBSs.

Three OldOBSs (K, L, M) were deployed so as to define a triangular network having equal sides, 10 km long, covering the North Anatolian Fault (Fig. 1). OBS L was placed on the bottom of the Tekirdag Basin, while OBS M was positioned in the northern part of the Tekirdag Basin, near WNW-ESE oriented normal faults [*Le Pichon et al.*, 2001; *Rangin et al.*, 2004], and OBS K was positioned on the southern side of the fault, in shallower water at a

depth of 546 m. Based on sediment sounder profiler (chirp) data, gas prone sediment layers were documented immediately below OBSs K and M [*Tary*, 2011].

The 5 remaining OBSs (OldOBS J, MicrOBS J2, ARMSS, NEEDLE and SPAN) were positioned near the foot of the southern flank of the Tekirdag Basin, at the center of the network, within a distance of ~100 to 400 m from a cold seep called "Jack the Smoker" sitting on the seafloor trace of the North Anatolian Fault [*Armijo et al.*, 2005; *Zitter et al.*, 2008]. These OBSs are very close from each other, the closest ones, ARMSS and SPAN, being separated by only 10 m (Fig. 1c).

3. Micro-events general characteristics and interpretation

The dataset was first analyzed to characterize the micro-seismicity in the area. The results were published in *Tary et al.* [2011]. Over the whole period, 270 seismic events (recorded at least at 3 stations) were identified using a STA/LTA detection algorithm (Short Term Average/Long Term Average).

The OBSs also recorded a large number of micro-events that were not detected by the above mentioned procedure, as they are generally not recorded by more than one station although their peak amplitude is comparable to the one of local micro-earthquakes (Fig. 3 and S3).

Generally, micro-events have: (1) short durations, ranging from 0.3 to 0.8 s in average, (2) frequency spectra between 4 and 30 Hz, (3) a large amplitude range of two orders of magnitude, and (4) no clear secondary arrival. Micro-events characteristics change slightly depending on the instrumental response of each OBS type (Fig. S3). Signals recorded by

OldOBSs have higher frequency contents (5-30 Hz) and shorter durations (0.1-0.6 s) than that of the other instruments (4-12 Hz, 0.5-0.8 s).

Except NEEDLE, all instruments have recorded micro-events (NEEDLE only recorded aseismic signals related to its post-penetration stabilization mainly during the first two days of the experiment), discarding the hypothesis of instrumental noise to explain their origin. The absence of micro-events in the NEEDLE records can be explained by the occurrence of gassy sediments directly in contact with the geophones. The additional impedance contrast at the surface of the buried pipe created by a thin film of fluid partially reflects the wave, and thus prevents this instrument to record the micro-events.

The micro-events are visible on the hydrophones only when these are close enough to the sediments surface. The hydrophones of ARMSS and J2, situated at the seafloor and ~30 cm above the seafloor, respectively, recorded only micro-events having amplitude on the vertical geophone exceeding ~2-3 µm/s (ARMSS) and ~15 µm/s (J2). Earthquakes and seismic shots with lower amplitudes on the vertical geophone (~1 µm/s) are clearly visible on all hydrophones. The absence or low amplitudes of the signals recorded by hydrophones appear to be specific to micro-events. This could be explained by a propagation mainly along the water-sediment interface, transmitting very little motions to the water column. Hydrophones from other OBSs (OldOBS and NEEDLE) would be too far from the water-sediment interface to be able to record any micro-events.

Figure 3

The micro-events are most of the time not correlated from one OBS to another, implying that the source is in very close vicinity of the OBS. Some strong micro-events are simultaneously recorded only by the closest stations, ARMSS and SPAN which are 10 m apart (Fig. S3). These pairs of signals present very different waveforms and frequency content likely due to

the strong resonance of OBS SPAN geophones around their natural frequency (4.5 Hz, Fig. S3). No location was attempted because of the poor quality of OBS SPAN recordings that involves large time picks uncertainties. On the other hand J2 and J, 25 m apart, did not record any correlated micro-events. The maximum spacing between two OBSs to simultaneously record micro-events of average amplitude is less than 10 m. Thus, micro-events seem to be strongly attenuated both horizontally in the sediments and vertically in the water column.

The number and temporal distribution of micro-events recorded by each instrument are shown in Table 1 and Fig. 4. About 7300 micro-events were detected. The number of micro-events is variable from one OBS to another. For instance, OBSs J and K, two OldOBSs with approximately the same recording period, recorded 915 and 3168 micro-events, respectively (Fig. 4 and Table 1).

No clear cycles, as the tidal cycles (less than 10 cm in the Sea of Marmara [*Alpar and Yüce*, 1997]), are visible on the micro-events temporal distribution. In addition, no clear correlation between the number of micro-events and the hour of the day has been found, as it could be expected if these signals resulted from the activity of some living organisms (Fig. S4).

Figure 4

Comparable non-seismic micro-events of short duration are very common on OBS recordings, but seismologists have paid little attention to these signals, as no useful correlation for seismological purposes can be made between distant instruments. *Buskirk et al.* [1981], *Diaz et al.* [2007] and *Sohn et al.* [1995] have reported very similar signals in varying environmental and geodynamical settings, i.e. the Pacific Rim borders, the Galicia passive margin, and the Southern Juan de Fuca ridge, respectively. These studies reported signals with: durations between 0.5 and 1 s in the case of *Diaz et al.* [2007] and *Sohn et al.* [1995], and between 0.5 and 4 s in the case of *Buskirk et al.* [1981]; frequency contents constituted by narrow peaks between 3 and 30 Hz; no clear secondary arrivals; and large differences in the

number of micro-events recorded by different OBSs. In addition, no correlation was found between micro-events recorded by 2 different OBSs. The signals reported by *Buskirk et al.* [1981] have longer durations in average, are monochromatic, and show a progressive decrease of the coda amplitude. The latter could be due to the instruments resonance, although *Buskirk et al.* [1981] also noticed that the frequency content of the recorded signals is different for the same OBS deployed at different sites.

The above observations rule out the hypothesis that the micro-events we observe could result from instrumental noise. *Buskirk et al.* [1981] claimed that the number of micro-events depends on the hour of the day for instruments at depths shallower than 1000 m. In addition, the number of events decreases with the depth of the instrument, suggesting a possible relationship with the vertical distribution of biomass in the ocean. Last but not least, no micro-events were recorded within boreholes, or other environments unfavorable for fish activity. These observations, and the recovery of living organisms (eggs of unknown origin) attached to two OBSs, lead *Buskirk et al.* [1981] to suggest a biological origin of the signals.

Another argument supporting the hypothesis of biological activity could be that the number of micro-events recorded by OldOBS K (water depth ~ 546 m) is two to three times greater than the number of micro-events recorded by OldOBSs J, L and M (water depth ~1000 m). However, besides biologic activity, pressure effects on gas bubbles can also explain the decrease in the number of micro-events with depth. Indeed, gas solubility decreases with pressure, resulting in an increase in bubble size and gas exsolution. Hence, for a same gas source and similar sediments, more bubbles will be created at lower pressure (i.e. at shallower depths). So, a decrease of biological activity is not the only parameter that could explain the decrease of the number of micro-events with depth.

Non-biological explanations for the micro-events are also far more likely for the following reasons. First, a total of 30 dives with Nautile submersible were conducted in 2007 to explore the Marmara deep seafloor [*Henry*, MarNaut cruise report, 2007], showing the relative scarcity of fish activity near the seabottom. Second, the occurrence of micro-events does not show any cyclicity, nor any clear dependence on the hour of the day (Fig. S4), while fish are supposed to have an internal biological clock [Bone and Moore, 2008]. Third, swarm of micro-events share relatively common characteristics (e.g. similar duration, frequency content, waveform), whatever the instrument design and during extended periods of time. As pointed out by *Diaz et al.* [2007], "the observation of events with very different amplitudes but very similar waveforms and the existence of clearly differentiated clusters of events, seem to discard a biological origin".

As mentioned earlier, the origin of the micro-events is very close to the instruments. Therefore, regional phenomena, such as tectonics or distant sources (e.g. related to human activity) can be discarded. In addition, sources in the water column (deep currents, resonating clouds of bubbles [*Pontoise and Hello,* 2002], T-waves [*Talandier and Okal*, 1996] and explosions/implosions) are very unlikely because micro-events were not recorded by OldOBS hydrophones. A relationship between deep currents and micro-events is also very unlikely because deep sea currents in the Sea of Marmara are, to some extent, a quasi steady state phenomenon, and cannot explain the characteristics of the observed micro-events.

On the other hand, gas is known to be common in marine sediments, and the Sea of Marmara is not an exception. Active venting sites have been found throughout the Sea of Marmara by geophysical means [*Alpar*, 1999; *Géli et al.*, 2008; *Dupré et al.*, 2010] and visual observations

[*Zitter et al.*, 2008]. A chirp profile, crossing the position of OBS J and M, was collected during the Marmesonet cruise in 2009 ([*Géli et al.*, 2010], Fig. 5). On this profile, a high-amplitude reflector followed by a strong attenuation of the seismic waves is clearly visible close to the fault situated below OBS M. These signatures are characteristic of the presence of gas. In addition, experiments and modeling [*Vidal et al.*, 2006; *Varas et al.*, 2009; *Diaz et al.*, 2007; *Chouet*, 1986, 1988, 1996; *Ferrazzini et al.*, 1990] of the opening and resonance of a cavity filled by fluids generate signals with waveforms qualitatively consistent with our data. Hence, in the following we suggest that the micro-events could result from gas migration in the seafloor, considering (i) the presence of gas and a fault near OBS M (where the swarm of micro-events was recorded); (ii) Modeling of source and wave propagation. The source of the micro-events is likely quite superficial, as no correlation is observed from one OBS to another, unless they are less than 15 m apart.

Figure 5

4. Specific cluster sequence on OBS M

4.1. Sequence chronology

Interestingly, OBS M recorded a swarm of 400 micro-events in 24 hours on June 11 and 12 (Fig. 6). Despite large amplitude differences, the micro-events recorded during this crisis have very similar waveforms (Fig. S5) and frequency contents (dominant frequency between 10 and 20 Hz). The number of micro-events increases gradually over the crisis, reaching a maximum after 6 hours with 96 micro-events in 2 hours (the background rate was ~ 5 micro-events/hour).

About two days before the swarm of micro-events, a very strong micro-event with a peak-to-peak amplitude >1000 µm/s was recorded by OBS M (Fig. 3a and 6). Despite its very high amplitude, the signal is not visible on the hydrophone.

As it occurred only ~40 minutes after OBS M hits the sea bottom (09/06/2007 17:48:04), it seems likely that the impact of the instrument on the seafloor has indirectly caused this strong signal. The impact may also have significantly destabilized the gas-prone sediments close to the OBS, causing gas expulsion from the superficial sediments. A similar process could also explain the increase in the number of micro-events just after the re-deployment of OBSs J, K and M.

Then, after about 40.5 h of relative quiescence, OBS M recorded the swarm. This phase constituted by signals of relatively low amplitudes could correspond to gas related processes within the superficial sediments.

Figure 6

4.2. Wave polarization analysis

First, the signals were detected with an automatic algorithm based on a STA/LTA threshold and visually controlled. Secondly, for each micro-event, one temporal series of *N* samples was extracted in order to control the origin time and average. The three-component temporal series in the OBS frame of reference were rotated in the wave frame of reference using a method based on *Jurkevics* [1988] for wave polarization analysis. The covariance matrix was calculated over the complete signal by

$$[S_{nm}] = \sum_{t=1}^{N} f_n(t)\, f_m(t) \quad , \qquad (1)$$

with N the number of samples, f the temporal series, and f_n and f_m the signal components on x, y or z.

Then, the eigenvectors ($\boldsymbol{u_1}$, $\boldsymbol{u_2}$ and $\boldsymbol{u_3}$) together with their corresponding eigenvalues (λ_1, λ_2, and λ_3) were determined from this symmetric 3 x 3 covariance matrix. The three pairs eigenvector-eigenvalue correspond to the polarization ellipsoid that best fit the data. As the type of waves corresponding to micro-events is not known *a priori*, the temporal series were only multiplied by the three eigenvectors in order to rotate the signals in the frame of reference of the polarization ellipsoid (components x1, x2, and x3) (Fig. 3).

In this frame of reference, the polarization of the micro-events presented in Fig. 3 is very different. In one case, the particle motion is mainly in the x1-x3 plane (Fig. 3a and 3c), which is consistent with surface waves (Stoneley-Scholte waves, e.g. *Favretto-Anrès and Rabau* [1997], *Zakharia* [2002]). In the other case, the particle motion is linear in the x1 direction (Fig. 3b), which in principle is consistent with both P- and S-waves. In addition, considering the frequency content of micro-events, the P- and S-waves velocities in superficial sediments (see section 5), and a realistic source-receiver distance of less than 15 m, near-field effects should dominate micro-events waveforms. These effects will ultimately make P- and S-waves arrivals undistinguishable [e.g. *Lokmer and Bean*, 2010]. Near-field effects also affect the polarization of body waves. Close to the source, both P- and S- waves can present *quasi-elliptical* polarization due to the superposition of near-field waves to the far-field wavetrains [*Vavryčuk*, 1992]. Thus, micro-events showing a non-linear polarization are not necessarily surface waves, but could also correspond to body waves significantly disturbed by the presence of near-field waves. This could explain the absence of the very high amplitude micro-event on hydrophone recordings if this signal is mainly composed by an S-wave (Fig. 3a). The source radiation pattern, which in principle could indicate which types of waves are expected depending on the source and receiver locations, was not used here due to the lack of information about the geometry of the source of micro-events.

Azimuths of the principal eigenvector $\boldsymbol{u_1}$ of the polarization ellipsoid for all micro-events of the swarm were obtained using

$$Az = \tan^{-1}\left(\frac{u_1(y)\,sign(u_1(z))}{u_1(x)\,sign(u_1(z))}\right). \quad (2)$$

The sign of the vertical component of the principal eigenvector is included in eq. 2 to resolve the 180° ambiguity in azimuths calculation. The azimuth of the signal presented in Fig. 3a, polarized in the x1-x3 plane, was determined by eq. (2) using only the horizontal components of $\boldsymbol{u_1}$. The 180° ambiguity in azimuths calculation was not resolved in this case. These azimuths in the OBS frame of reference are shown in Fig. 7. The orientation of the principal eigenvector is very stable over the crisis, around 285° – 315° in the OBS frame of reference, suggesting a localized source. Azimuths calculated for the other two eigenvectors show no preferential orientation, as expected if very little wave energy is focused on these components. Noticeably, the strong micro-event and the micro-events constituting the swarm recorded by OBS M have similar azimuths, 294° [180°] and 285° – 315°, respectively. One possibility is that both could be related to fluid migration along the fault that is visible on the chirp profile located close to OBS M (Fig. 5).

Figure 7

4.3. Principal Component Analysis (PCA)

In order to find the common features of micro-events and propose some physical explanations, a PCA was applied to determine the most characteristic micro-events of the swarm. Prior to the calculation of the PCA, the signals were rotated in the frame of reference of the polarization ellipsoid following the method described in section 4.2. The covariance matrix between all signals, with a common origin and a zero-average, was calculated following this formula,

$$\left[C_{tp,tq}\right] = \sum_{1 \le i,j \le M} f_i(t_p)\, f_j(t_q) \text{ where } t_1 \le t_p, t_q \le t_N, \quad (3)$$

with f_i and f_j the temporal series, M the number of micro-events, and N the number of samples.

Eventually, the characteristic signals (eigenvectors, $\boldsymbol{V_i}$, i = 1, M) and their data representativeness (eigenvalues, λ_i, i = 1, M) are calculated from the covariance matrix. Hereafter, the representativeness of each eigenvector will be given as a percentage of the total energy ($\lambda_i^2/\Sigma\lambda_i^2$).

The micro-events constituting the swarm recorded by OBS M on June 11 and 12 present four particularities: (i) they are very impulsive; (ii) of short duration (mainly around 0.1 s); (iii) very similar; (iv) and present higher amplitudes on the horizontal components than on the vertical one (Fig. 3b). The PCA performed with this dataset indicates that the first eigenvector has a data representativeness of ~83 % on the x1 component (Fig. 8), suggesting a common source and similar source-receiver ray paths. The relatively low data representativeness of the first eigenvectors of the x2 and x3 components, ~35 and 58 %, respectively, result likely from the presence of coherent arrivals of smaller amplitudes, such as near-field waves, modifying the otherwise linear polarization of these micro-events.

The characteristic signal is very impulsive and has a duration around 0.15 s on the x1 component. Frequency spectra of the eigenvectors of the three components show one main peak between 13 and 20 Hz. Noticeably, the frequency spectrum of the first eigenvector of the x1 component show a higher frequency content than the other components (Fig. 8). The main characteristics of the first eigenvectors are summarized in Table 2.

Table 2

Figure 8

The PCA was also applied to the complete dataset. Most of the first eigenvectors have a frequency spectrum with one dominant frequency, between 5 and 23 Hz for Ifremer OBSs (J,

K, L, M, and J2) and around 10 Hz for OBS ARMSS (Table S2 and Fig. S6). Considering only the x1 component, more than 80% of the micro-events energy corresponds to the first five eigenvectors (i.e. five families). The micro-events could then be grouped in families as in *Diaz et al.* [2007], the characteristics of these families being slightly different from one OBS to another (Fig. S6).

5. Source and wave propagation modeling

The numerical simulations were carried out using the SKB code [*Dietrich*, 1988]. This code computes, as a function of frequency and wave number, the response in terms of stress and displacement of a 3D, horizontally stratified, half-space subjected to a source positioned anywhere in the stratification. Fluid layers within or bounding the stratification can be taken into account. The attenuation is included by working with complex wave velocities [*Toksöz and Johnston*, 1981]. The computation is based on a recursive algorithm using reflection-transmission coefficients as wave vector propagators [*Kennet and Kerry*, 1979]. The last steps of the computation are to integrate in discrete wave numbers [*Bouchon*, 1981], and to make a convolution with a spectrum of a signal source followed by an inverse Fourier transform in time, in order to recover stresses and displacements in space and time.

According to *Biot* [1956], water saturation induces an attenuation that can be accounted for by a complex formulation of wave velocities, as in visco-elastic media (see also *Géli et al.* [1987]). Therefore, our computation method is adapted to the modeling of wave propagation in strongly attenuating, marine sub-surface sediments, [e.g. *Meunier and Guennou*, 1991]. This computation method takes into account the complete wave field (direct, transmitted, and

reflected waves), including both far-field and near-field terms [*Dietrich and Bouchon*, 1985]. The representation of the source in terms of forces or moment tensor appears within the SKB code in terms of equivalent stress or displacement discontinuity, allowing the calculation of stress and displacement at the receivers by using reflection-transmission coefficients. The source signal used is the zero-phase Ricker signal.

The model consists of a 1110 m thick water layer, with typical density of 1000 kg/m^3 and P-wave velocity of 1500 m/s, overlying a homogeneous half-space. Sediments P-wave velocity and density measured on cores (using a Geotek Multi-Sensor Core Logger - MSCL) collected near OBS J have been used for the numerical seismograms calculation (Fig. S7). The acoustical properties of the homogeneous half-space correspond to those of a soft and very attenuating sediment, i.e. a density of 1500 kg/m^3, P-wave velocity and quality factor of 1550 m/s and 10, S-wave velocity and quality factor of 100 m/s [*Sultan et al.*, 2007] and 10 [*Wang et al.*, 1994; *Campbell*, 2009]. Three types of point source were tested: an isotropic explosive source generating P-waves with the same energy in all directions, and two unidirectional forces generating P-waves with the maximum of energy in the horizontal and vertical directions. A two-component source (isotropic and single force) in an elastic half-space was studied by *Kanamori et al.* [1984] for the case of the rupture of a "lid" on top of a cylinder. In the near-field, they show that the isotropic part of the source can be neglected when the radius of the cylinder is small compared to the source-receiver distance. In our case, the conduits radius, inferred from the bubble size at the seafloor, is less than 1 cm, while the source-receiver distance ranges between 1 and 10 m, resulting in a ratio of ~0.001-0.01. Hereafter, the waveform modeling using an isotropic source is given for comparison.

In all simulations, the source signal has a constant frequency content of 15 Hz, consistent with the observed micro-event frequency content. Numerical seismograms were calculated for 100 horizontally aligned receivers (spaced by 1 m) at four different depths (0.01 m below and 0.1,

0.3, 0.9 m above the water-sediment interface), and two source depths, 2 and 5 m below the water-sediment interface (Fig. 9).

Figure 9

Whatever the type and depth of the source, the computed signals are attenuated very quickly in the sediments (Fig. 10). Surface waves (Stoneley-Scholte waves) are produced by both unidirectional forces and the explosive source in superficial sediments. These waves, propagating at ~77 m/s in our configuration, are attenuated both horizontally in sediments and vertically in the water column (Fig. 10 and 11). However, in the case of an explosive source, P-waves with significant amplitudes are clearly visible on the horizontal component.

The micro-event shown in Fig. 3c has about the same amplitude on the x1 component than on the x3 component, which could be compatible with Stoneley-Scholte waves produced by a shallow source.

The impulsive micro-events of the crisis have most of their energy on the x1 component and thus cannot be interpreted as Stoneley-Scholte waves (Fig. 3b). They could in principle be better explained by a P or an S-wave hitting the sediments-water interface with a high incidence angle, transmitting little energy to the water column. The corresponding wavelength would be of the order of 100 m and 6.7 m, respectively, which is probably much more than, or in the order of, the distance to the source. Most likely, these impulsive signals are generated by a weak but very close source causing horizontal displacement, which could be a pulsing conduit.

Figure 10

Figure 11

6. Physical hypotheses and interpretation

6.1. Physical hypotheses

Bubbles in sands are spherical, grow and migrate by displacing grains, whereas bubbles in clay are presumably oblate spheroid, and migrate by fracturing the sediments [*Johnson et al.*, 2002; *Boudreau et al.*, 2005]. Hence, gas migration in fine-grained sediments is expected to depend on fracture propagation, which is a function of the mechanical properties of the medium through its Young's modulus *E*, shear strength, and fracture toughness K_{1c} [*van Kessel and van Kesteren*, 2002; *Algar et al.*, 2009]. However, it is often observed at the seafloor that bubbles escape continuously through tubular conduits, which are sometime recovered by cemented chimneys in the sediments. Such open conduits may be maintained to a few meters depth in the sediment and enable bubble-induced pore water mixing [*Haeckel et al.*, 2007].

Laboratory experiments, where gas (air) is injected in a granular media (sodosilica grains with diameters of 100 and 400 µm), have shown that gas escapes through numerous conduits that look like tree branches [*Varas et al.*, 2009; *Varas et al.*, 2011]. Gas conduits seem to be intrinsically unstable, because, even without variations of the gas injection rate, conduits are created or closed continuously. The superficial sediments of the Sea of Marmara are mainly clay-rich cohesive sediments with particles smaller than 5 µm. Nevertheless, open conduits in compacting sediments are expected to be mechanically unstable except very close to the seafloor. We suspect that the opening and collapse of conduits or gas filled fractures could explain the characteristics of micro-events (Fig. 3). Considering the low cohesion of superficial sediments, the vertical force needed by the fluids to move up toward the seafloor is supposedly small. The main displacements are then produced by the side walls of the sub-vertical conduit. In addition, the conduits observed during laboratory experiments of gas injection in granular media [*Varas et al.*, 2009; *Varas et al.*, 2011] are generally nearly verticals. Explosion or vertical force types of source are still possible if a layer of higher cohesion is present on the pathway of the gas.

Then, our preferred mechanism consists of a sub-vertical fracture, pre-existent or not, gradually filled by gas within a porous and saturated medium (Fig. 12). The fracture is located close to the sediment-water interface. Gas pressure increases as the crack fills and progressively opens (step 0). When the fracture toughness threshold is reached, the gas will rise up in a moving crack, reaching or not the sediment-water interface (step 1), where it can escape to the seawater (step 2) without major deformation of the sedimentary matrix [*Johnson et al.*, 2002; *Boudreau et al.*, 2005; *Algar et al.*, 2009]. After the gas migration, the confining pressure will close the fracture. Fluid-filled crack models don't require venting, but focus mainly on the resonance characteristics of the cracks [e.g. *Aki et al.*, 1977; *Chouet*, 1986, 1988; *Jousset et al.*, 2003]. Hence, micro-events can be generated as the gas migrates in the conduit, or by its expulsion at the seafloor. The partitioning of the signal recorded by the OBSs in horizontal and vertical motions will depend on fractures tilt and depth, and on wave propagation processes.

Figure 12

6.2. Interpretation of the micro-events crisis

We identified two types of micro-events: small impulsive, clustered events and larger amplitude oscillatory signals, which appear less frequently and display more variability and could correspond to Stoneley-Scholte waves.

Varas et al. [2009] described two regimes of bubbles emission in granular media depending on the gas injection rate. At low flow rate, large and independent bubbles are formed ("bubbling regime"), whereas at high flow rate, small bubbles supplied by a continuous channel are produced ("open-channel regime"). Except the swarm recorded by OBS M, all OBSs displayed a low daily rate of micro-events. We propose that the larger micro-events correspond to the collapse of a cavity or fracture that trapped gas at a relatively shallow depth

below the sediments. The crisis recorded by OBS M followed such an event and could, hypothetically, result from a nearby continuous flow of bubbles in an open-channel regime which followed the expulsion of the gas from the main cavity.

7. Conclusions

Numerous non-seismic micro-events of short durations were recorded on different types of OBSs. These signals, of peak amplitudes comparable to those of earthquakes, were predominantly recorded by geophones. They were also recorded by those hydrophones situated less than a few tens of centimeters from the seafloor. Because the signals have similar characteristics (terms of duration, frequency content), whatever the instrument and whatever the environment, it is very unlikely -if not impossible- that these micro-events be related to instrumental artifacts, or “fish bumps”.

The micro-events are generally not correlated from one OBS to another, with one noticeable exception for the closest OBSs (~10 m apart). Moreover, micro-events present a specific attenuation pattern, i.e. both horizontally in sediments and vertically in the water column.

Specific focus has been given to the micro-events recorded by OBS M during the crisis that occurred on June 11-12, 2007. The presence of gas in the superficial layers and the source modeling we performed suggest that these micro-events are likely related to gas related processes from the seafloor, such as the opening and closure of a conduit induced by degassing near the subsurface. The present work shows that OBSs can detect episodes of gas accumulation and release in shallow sediment layers. In combination with piezometers and

bubble recorders, OBS could be used in the Sea of Marmara to monitor the evolution of such episodes, hence to better understand the relationships between deformation and non-seismic transients related to degassing from the sub-seafloor layers near the fault zone.

Our work also confirm recent results obtained with multibeam acoustic systems operating in the water column mode, suggesting that free gas emissions from the seafloor are likely to be more widespread than previously thought.

8. Acknowledgements

This work is part of PhD Thesis of J. B. Tary, co-funded by Total, Magnitude/BakerHughes and Ifremer. CGGVeritas kindly provided the data from the ARMSS, NEEDLE and SPAN. The work was conducted within the Marmara Demonstration Mission of the European Seafloor Observatory Network (ESONET) and benefited from financial support from both ESONET and Agence Nationale de la Recherche (project ANR/ISIS). Special acknowledgments to: Captain and crew of Ifremer and ITU vessels (R/V L'Atalante and R/V Yunuz) ; Francis Cerda (Total), Thomas Bardainne (Magnitude, BakerHughes) ; Renaud Daures, Emmanuel Auger (CGGVeritas) ; Bach-Lien Hua, Pascal Pelleau, Ronan Apprioual and Yves Auffret (Ifremer) ; Jacques Talandier, and Michel Dietrich.

9. References

Aki, K., Fehler, M., & Das, S., 1977. Source mechanism of volcanic tremor: fluid-driven crack models and their application to the 1963 Kilauea eruption, *Journal of Volcanology and Geothermal Research, 2*, 259-287.

Algar, C. K. & Boudreau, B. P., 2009. Transient growth of an isolated bubble in muddy, fine grained sediments, *Geochim. Cosmochim. Acta, 73*, 2581-2591, doi: 10.1016/j.gca.2009.02.008.

Alpar, B., 1999. Underwater signatures of the Kocaeli earthquake of 17 August 1999 in Turkey, *Turkish J. Mar. Sci., 5*, 111-130.

Alpar, B. & Yüce, H., 1997. Short and tidal period sea-level variations along the Turkish Strait system, *Turkish J. Mar. Sci., 3*, 11-22.

Armijo, R., Pondard, N., Meyer, B., Uçarkus, G., Mercier de Lépinay, B., Malavieille, J., Dominguez, S., Gustcher, M.-A., Schmidt, S., Beck, C., Çagatay, N., Çakir, Z., Imren, C., Eris, K., Natalin, B., Özalaybey, S., Tolun, L., Lefèvre, I., Seeber, L., Gasperini, L., Rangin, C., Emre, O. & Sarikavak, K., 2005. Submarine fault scarps in the Sea of Marmara pull-apart (North Anatolian Fault): implications for seismic hazard in Istanbul, *Geochem. Geophys. Geosyst., 6*, Q06009, doi: 10.1029/2004GC000896.

Biot, M. A., 1956. Theory of the propagation of elastic waves in a fluid saturated porous solid, 1, Low-frequency range, *J. Acoustic Soc. Am., 28*, 168-178.

Bone, Q., and Moore, R. H., 2008. Biology of fishes, 3rd edition, Auflage, Taylor & Francis, 478p.

Bouchon, M., 1981. A simple method to calculate Green's functions for elastic layered media, *Bull. Seism. Soc. Am., 71,* 959-971.

Boudreau, B. P., Algar., C., Johnson, B. D., Croudace, I., Reed, A., Furukawa, Y., Dorgan, K. M., Jumars, P. A., Grader, A. S. & Gardiner, B. S., 2005. Bubble growth and rise in soft sediments, *Geology, 33(6),* 517-520, doi: 10.1130/G21259.1.

Bourry, C., Chazallon, B., Charlou, J. L., Donval, J. P., Ruffine, L., Henry, P., Geli, L., Çagatay, N., İnan, S. & Moreau, M., 2009. Free gas and gas hydrates from the Sea of Marmara, Turkey. Chemical and structural characterization, *Chemical Geology, 264,* 197-206, doi: 10.1016/j.chemgeo.2009.03.007.

Buskirk, R.E., Frohlich, C., Latham, G. V., Chen, A. T. & Lawton, J., 1981. Evidence that biological activity affects ocean bottom seismograph recordings, *Mar. Geophys. Res., 5 (2),* 189-205.

Campbell, K. W., 2009. Estimates of shear-wave Q and κ0 for unconsolidated and semiconsolidated sediments in Eastern North America, *Bull. Seism. Soc. Am., 99,* 2365-2392, doi: 10.1785/0120080116.

Chouet, B., 1986. Dynamics of a Fluid-Driven Crack in Three Dimensions by the Finite Difference Method, *J. Geophys. Res., 91(B14),* 13967-13992.

Chouet, B., 1988. Resonance of fluid-driven crack : radiation properties and implications for the source of long-period events and harmonic tremor, *J. Geophys. Res., 93*, 4375-4400.

Chouet, B., 1996. Long-period volcano seismicity : its source and use in eruption forecasting, *Nature, 380*, 309-316, doi: 10.1038/380309a0.

Diaz, J., Gallart, J. & Gaspà, O., 2007. Atypical seismic signals at the Galicia Margin, North Atlantic Ocean, related to the resonance of subsurface fluid-filled cracks, *Tectonophysics, 433*, 1-13, doi: 10.1016/j.tecto.2007.01.004.

Dietrich, M., 1988. Modeling of marine seismic profiles in the t-x and tau-p domains, *Geophysics, 53*, 453-465, doi: 10.1190/1.1442477.

Dietrich, M. & Bouchon, M., 1985. Synthetic vertical seismic profiles in elastic media, *Geophysics, 50(2)*, 224-234.

Dupré, S., Scalabrin, C., Géli, L., Henry, P., Grall, C., Tary, J. B., Çagatay, N., Imren, C. & the MARMESONET Scientific Party, 2010. Widespread gas emissions in the Sea of Marmara in relation with the tectonic and sedimentary environments: results from shipborne multibeam echosounder water column imagery (MARMESONET expedition, 2009), EGU General Assembly, Vienna, Abstract EGU2010-9429-2.

Favretto-Anrès, N., & Rabau, G., 1997. Excitation of the Stoneley-Scholte wave at the boundary between and ideal fluid and a viscoelastic solid, *J. Sound and Vibration, 203(2),* 193-208.

Ferrazzini, V., Chouet, B., Fehler, M. & Aki, K., 1990. Quantitative analysis of long-period events recorded during hydrofracture experiments at Fenton Hill, New Mexico, *J. Geophys. Res., 95(B13),* 21871-21884.

Géli, L., Bard, P.-Y. & Schmitt, D. P., 1987. Seismic wave propagation in a very permeable water-saturated surface layer, *J. Geophys. Res., 92,* 7931-7944.

Géli, L., Henry, P., Zitter, T., Dupré, S., Tryon, M., Çagatay N. M., Mercier de Lépinay, B., Le Pichon, X., Şengör, A.M.C., Görür, N., Natalin, B., Uçarkuş, G., Özeren, S., Volker, D., Gasperini, L., Bourlange, S. & the Marnaut Scientific Party, 2008. Gas emissions and active tectonics within the submerged section of the North Anatolian Fault zone in the Sea of Marmara, *Earth Planet. Sci. Lett., 274,* 34-39, doi: 10.1016/j.epsl.2008.06.047.

Géli, L., Henry, P. & Çagatay, N., 2010. Marmesonet Leg1 Cruise Report, November 4th – November 25th, 2009, http://www.esonet.marmara-dm.itu.edu.tr/ (12,2010).

Haeckel, M., Boudreau, B. P. & Wallmann, K., 2007. Bubble-induced porewater mixing: A 3-D model for deep porewater irrigation, *Geochim. Cosmochim. Acta, 71,* 5135-5154, doi: 10.1016/j.gca.2007.08.011.

Halbach, P., Holzbecher, E., Reichel, T. & Moche, R., 2004. Migration of the sulphate-methane reaction zone in marine sediments of the Sea of Marmara – can this mechanism be tectonically induced ?, *Chemical Geology, 205,* 73-82, doi: 10.1016/j.chemgeo.2003.12.013.

Henry, P. and MarNaut Cruise Sci. Party, 2007, MarNaut Cruise of R/V L'Atalante Report, http://cdf.u-3mrs.fr/~henry/marmara/marnaut_public/marnaut_final_reports/.

Imren, C., Le Pichon, X., Rangin, C., Demirbağ, E., Ecevitoğlu, B. & Görür, N., 2001. The North Anatolian Fault within the Sea of Marmara: a new interpretation based on multichannel seismic and multi-beam bathymetry data, *Earth Planet. Sci. Lett., 186,*143–158, doi: 10.1016/S0012-821X(01)00241-2

Johnson, B. D., Boudreau, B. P., Gardiner, B. S. & Maass, R., 2002. Mechanical response of sediments to bubble growth, *Marine Geology, 187,* 347-363.

Jousset, P., Neuberg, J., & Sturton, S., 2003. Modelling the time-dependent frequency content of low-frequency volcanic earthquakes, *Journal of Volcanology and Geothermal Research, 128,* 201-223, doi: 10.1016/S0377-0273(03)00255-5.

Jurkevics, A., 1988. Polarization analysis of three-component array data, *Bull. Seism. Soc. Am., 78,* 1725-1743.

Kanamori, H., Given, J. W., & Lay, T., 1984. Analysis of Seismic Body Waves Excited by the Mount St. Helens Eruption of May 18, 1980, *J. Geophys. Res., 89(B3),* 1856-1866.

Le Pichon, X., Şengör, A. M. C., Demirbağ, E., Rangin, R., Imren, C., Armijo, R., Görür, N., Çağatay, N., Mercier de Lepinay, B., Meyer, B., Saatcilar, R. & Tok, B., 2001. The main Marmara fault, *Earth Planet. Sci. Lett., 192,* 595-616.

Lokmer, I. & Bean, C. J., 2010. Properties of the near-field term and its effect on polarization analysis and source locations of long-period (LP) and very-long-period (VLP) seismic events at volcanoes, *Journal of Volcanology and Geothermal Research, 192*, 35-47.

Kennet, B. L. N. & Kerry, N. J., 1979. Seismic waves in a stratified half-space, *Geophys. J. Roy. Astr. Soc., 57,* 557-583.

Meunier, J. & Guennou, C., 1991. Computation of shear waves by integral methods in stratified media, in *Shear waves in Marine Sediments*, pp. 495-502, edited by J. M. Hovem et al., Kluwer Academic Publishers, printed in the Netherlands.

Pontoise, B. & Hello, Y., 2002. Monochromatic infra-sound waves recorded offshore Ecuador : possible evidence of methane release, *Terra Nova, 14*, 425-435.

Rangin, C., Demirbağ, E., Imren, C., Crusson, A., Normand, A., Le Drezen, E. & Le Bot, A., 2001. Marine Atlas of the Sea of Marmara (Turkey), IFREMER, France.

Rangin, C., Le Pichon, X., Demirbağ, E. & Imren, C., 2004. Strain localization in the Sea of Marmara: propagation of the North Anatolian Fault in a now inactive pull-apart, *Tectonics, 23(2)*, TC2014, doi: 10.1029/2002TC001437.

Sohn, R. A., Hildebrand, J. A., Webb, S. C. & Fox, C. G., 1995. Hydrothermal activity at the Megaplume Site on the Southern Juan de Fuca Ridge, *Bull. Seism. Soc. Am.*, *85(3)*, 775-786.

Sultan, N., Voisset, M., Marsset, T., Vernant, A. M., Cauquil, E., Colliat, J. L. & Curinier, V. 2007. Detection of free gas and gas hydrate based on 3D seismic data and cone penetration testing: An example from the Nigerian Continental Slope, *Marine Geology, 240*, 235-255, doi:10.1016/j.margeo.2007.02.012.

Talandier, J. & Okal, E. A., 1996. T waves from underwater volcanoes in the Pacific Ocean: ringing witnesses to geyser processes ?, *Bull. Seismol. Soc. Am., 86(5)*, 1529-1544.

Tary, J. B., 2011. *Case studies on fluids and seismicity in submarine environments based on Ocean Bottom Seismometers (OBS) recordings from the Sea of Marmara and application to the Niger Delta*, PhD Thesis, Université de Bretagne Occidentale. http://archimer.ifremer.fr/doc/00034/14557/

Tary, J. B., Géli, L., Henry, H., Natalin, B., Gasperini, B., Çomoglu, M., Çagatay, N. & Bardainne, T., 2011. Sea bottom observations from the western escarpment of the Sea of Marmara, *Bull. Seismolog. Soc. Am.*, *101*, 775-791, doi: 10.1785/0120100014.

Toksöz, M. N. & Johnston, D. H., eds., 1981. Seismic wave attenuation, *Geophysics Reprint Series, No. 2*, Society of Exploration Geophysicists, Tulsa, OK.

van Kessel, T. & van Kesteren, W. G. M., 2002. Gas production and transport in artificial sludge depots, *Waste Management, 22*, 19-28.

Varas, G., Vidal, V. & Géminard, J. C., 2009. Dynamics of crater formations in immersed granular materials, *Phys. Rev. E., 79*, 021301, doi: 10.1103/PhysRevE.79.021301.

Varas, G., Vidal, V. & Géminard, J. C., 2011. Venting dynamics of an immersed granular layer, *Phys. Rev. E., 83*, 011302, doi: 10.1103/PhysRevE.83.011302.

Vavryčuk, V., 1992. Polarization properties of near-field waves in homogeneous isotropic and anisotropic media: numerical modeling, *Geophys. J. Int., 110*, 180-190.

Vidal, V., Géminard, J.-C., Divoux, T. & Melo, F., 2006. Acoustic signal associated with the bursting of a soap film which initially closes an overpressurized cavity, *Eur. Phys. J. B., 54*, 321-329, doi: 10.1140/epjb/e2006-00450-0.

Wang, Z., Street, R., Woolery, E. & Harris, J., 1994. *Qs* estimation for unconsolidated sediments using first-arrival *SH* wave critical refractions, *J. Geophys. Res., 99*, 13543-13551.

Zakharia, M. E., 2002. Sub-bottom variability characterization using surface acoustic waves, in *Impact of Littoral Environmental Variability on Acoustic Predictions and Sonar Performance*, edited by N. G. Pace and F. B. Jensen, pp. 131-138.

Zitter, T.A.C., Henry, P., Aloisi, G., Delaygue, G., Çagatay, M.N., Mercier de Lepinay, B., Al-Samir, M., Fornacciari, F., Tesmer, M., Pekdeger, A.,Wallmann, K. & Lericolais, G., 2008. Cold seeps along the main Marmara Fault in the Sea of Marmara (Turkey), *Deep-Sea Res., 55*, 552-570, doi:10.1016/j.dsr.2008.01.002.

10. Figure captions

Figure 1. (a) Map of the Sea of Marmara with active fault traces [*Rangin et al.*, 2001, 2004; *Imren et al.*, 2001; *Armijo et al.*, 2005]. Abbreviations: NAFZ, North Anatolian Fault Zone; TB, Tekirdag Basin; WH, Western High; CB, Central Basin; KB, Kumburgaz Basin; CH, Central High; ÇB, Çinarcik Basin; IB: Imrali Basin; P., Peninsula; Is., Island. (b) Bathymetric map of the Tekirdag Basin. OldOBSs deployed during the MarNaut cruise in 2007 are indicated by black triangles. The black line with numbers corresponds to the ship track and trace numbers of the chirp profile in Fig. 5. The faults are indicated by the other black lines. (c) Zoom in the OBS network center. Microbathymetric data were acquired during the MARMARASCARPS cruise in 2002 by the R.O.V. Victor [*Armijo et al.*, 2005]. OBSs provided by Ifremer and CGGVeritas are indicated by black triangles and black dots, respectively. The black star shows the location of "Jack the Smoker" site where fresh water escapes from the seafloor through carbonate chimneys. The photograph taken by the R.O.V. Victor on the seafloor shows the outflow of fresh water as well as a fish on top of the main chimney. The white part of the chimney corresponds to bacterial mats. The black diamond shows the location of the seismic shot used for OBSs amplitude inter-calibration (see Fig. S2).

Figure 2. Schematic structure of the OBSs deployed during the MarNaut cruise. For each OBS, the hydrophone location is indicated by the gray rectangle. ME: micro-events.

Figure 3. Three examples of micro-events recorded by OBS M and OBS K. The three-components seismograms are presented before (H: hydrophone, X and Y: horizontal components, Z: vertical component) and after rotation in the frame of reference of the polarization ellipsoid (components x1, x2 and x3). Azimuths were calculated using eq. (2) (see section 5.2 for explanations). a) Micro-event recorded by OBS M on 09 June 2007 at 18:27:55 with corrected amplitudes of few hundreds of µm/s. b) Micro-event recorded by OBS M on 11 June 2007 at 17:43:08 with corrected amplitudes of a few µm/s. This micro-event is typical of the ones constituting the swarm. Note that the two micro-events have similar azimuth. c) Micro-event recorded by OBS K on 16 May 2007 at 00:10:47 with corrected amplitudes similar to the micro-event presented in b). Amplitudes were corrected according to the methodology described in section 2. Note the difference in polarization between the micro-events shown in a) and c) (plane x1-x3), and the micro-event shown in b) (component x1).

Figure 4. Temporal evolution of the number of micro-events recorded by OBSs J, K, L, M, ARMSS, J2 and SPAN. N_{ME}: number of micro-events.

Figure 5. Chirp profile acquired during the MARMESONET cruise in Nov.-Dec. 2009 ([*Géli et al.*, 2010], see location in Fig. 1). OBSs J and M are indicated on the profile by black triangles. Below M is visible a high amplitude reflector followed by a strong attenuation of the seismic waves (zoom on the right). No seismic anomaly is visible below J (zoom on the left).

Figure 6. (a) Recordings of OBS M during the crisis of micro-events, 11/06 12:00 – 12/06 06:00 (H: Hydrophone, X and Y: horizontal geophones, Z: vertical geophone). Peak-to-peak

amplitudes of the micro-events recorded on OBS M for the x1 component: b) three-days sequence after deployment (2007 June 10-2007 June 13); (c) during the crisis.

Figure 7. Azimuths of the first eigenvector of the polarization ellipsoid in the OBS frame of reference determined for the micro-events constituting the crisis recorded on OBS M. OBS horizontal components X and Y are directed toward 0 and 90 degrees, respectively. Numbers near the dotted circles inside the diagram indicate the number of micro-events. Each gray bin represents 5 degrees. The azimuth of the high amplitude micro-event presented in Fig. 3a (294° [180]) is indicated by the black dot. This event being possibly a S-wave significantly affected by near-field waves or an interface wave, the 180° ambiguity in azimuths calculation was not resolved (white-dashed dot).

Figure 8. PCA of the micro-events constituting the crisis identified on OBS M for the components x1, x2 and x3. a) Representativeness of the first 10 eigenvectors. b) Temporal series of the first eigenvectors. The representativeness of each eigenvector is indicated by its eigenvalue given in percentage of the total energy. The eigenvector spectrum is given on the right.

Figure 9. Configuration of the model used for micro-event modeling. A point source (unidirectional force or explosive) located in a homogeneous half space produces either P- or interface waves recorded by a set of equally-spaced receivers on the surface (4 sensor heights: 0.01 below and 0.1, 0.3 and 0.9 m above the interface).

Figure 10. Numerical simulations using the SKB code [*Dietrich*, 1988] for a horizontal, a vertical and an explosive source located at 2 m bsf (below sea floor), and sensors 1 cm within

the sediments. The original numerical signals in displacement were differentiated once (velocity) and then normalized by the first numerical signal (distance: 10 m). H: horizontal motion; Z: vertical motion. Note the strong attenuation of P- and surface waves.

Figure 11. a) Micro-events numerical simulations for a horizontal source at 2 m bsf and sensors at 0.1, 0.3 and 0.9 m above the interface (distance: 10 m), showing the vertical attenuation of surface waves. b) Hydrophone recordings of OBSs ARMSS (~0.05 m), J2 (~0.3 m) and J (~0.9 m), for three signals of similar corrected amplitudes (~15 µm/s) recorded by these OBSs. The signals are normalized by those situated close to the seawater-sediments interface (0.1 m – ARMSS).

Figure 12. Schematic explanation in 3 steps of the mechanism proposed for the micro-events source: gas migration and escape through a sub-vertical conduit.

11. Tables

Stations	Long. (deg)	Lat. (deg)	Depth (m)	Recording period	F_0 (Hz)	Fs (Hz)	Observations	N_{ME}	N_{ME}/day
J	E 27.62921	N 40.80372	1112	14 May - 30 Aug. 2007	4.5	250		915	8
J2	E 27.62902	N 40.80390	1112	22 May - 28 May 2007	4.5	250	X comp. resonance	43	7
K	E 27.6608	N 40.7613	546	14 May - 19 Aug. 2007	4.5	250		3168	33
L	E 27.5645	N 40.8044	1132	14 May - 09 June 2007	4.5	250		461	18
M	E 27.6637	N 40.8466	1110	14 May - 26 Aug. 2007	4.5	250		1534	15
ARMSS	E 27.62774	N 40.80382	1115	14 May - 09 June 2007	14	500		1079	42
SPAN	E 27.62782	N 40.80376	1117	14 May - 28 May 2007	4.5	500	Low quality	85	6
NEEDLE	E 27.62714	N 40.80337	1115	14 May - 28 May 2007	4.5	500		0	0

Table 1. Position, technical characteristics, recording period, number of micro-events recorded (N_{ME}) and N_{ME} per day for each OBS. F_0: geophones natural frequency; Fs : sampling frequency; comp.: component.

	Eigenvector 1		
Components	%	Freq. (Hz)	Dur. (s)
OBS M swarm (368 ME)			
x1	83	13 - 20	0.14
x2	35	14.2	0.21
x3	58	14.5 - 17	0.23

Table 2. First eigenvector characteristics of the PCA performed on the micro-events of the swarm recorded by OBS M. The number of micro-events used in the PCA is also indicated (ME: micro-events). %: data representativeness (energy); Freq.: dominant frequency; Dur.: duration.

12. Figures

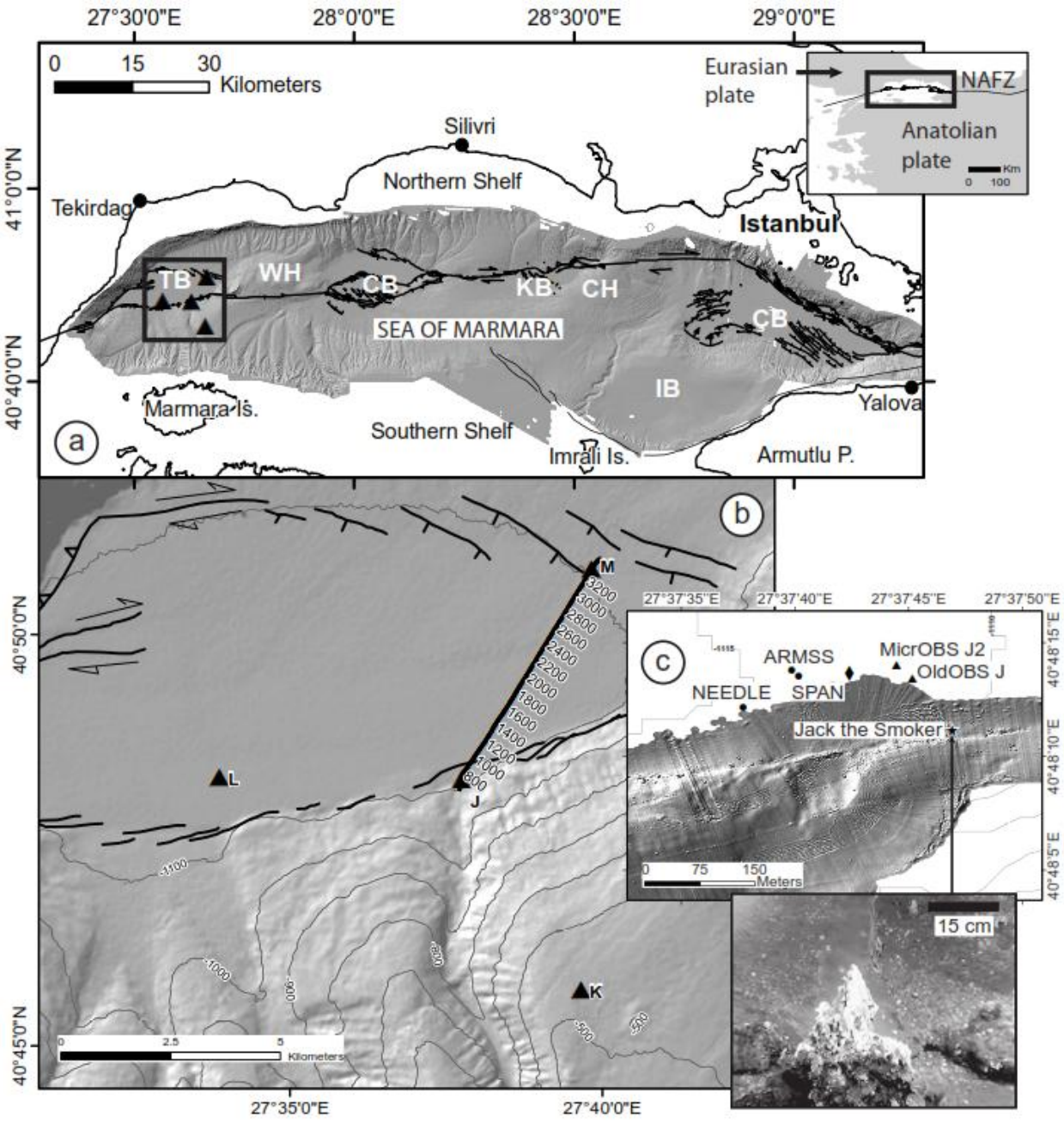

Figure 1

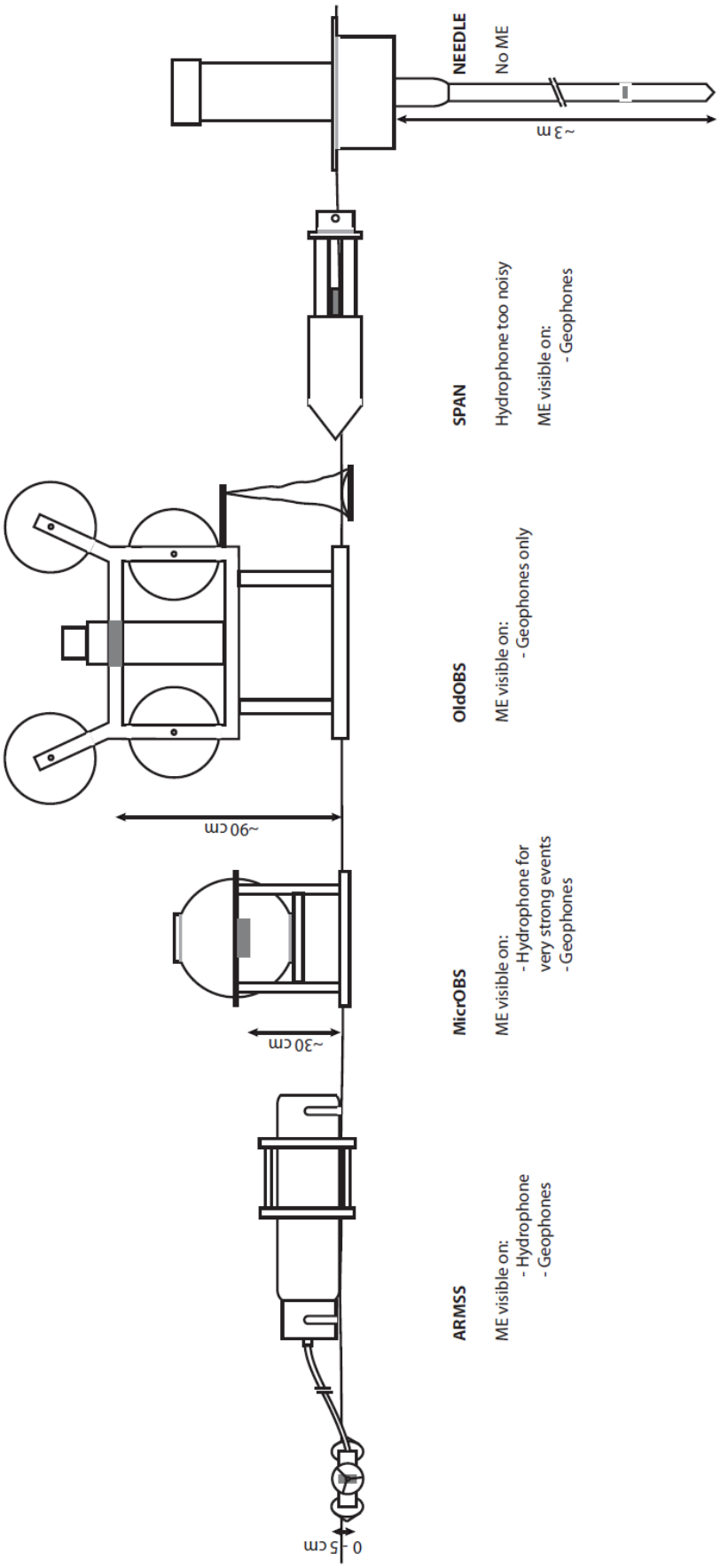
NEEDLE
No ME
~3 m
SPAN
Hydrophone too noisy
ME visible on:
- Geophones
OldOBS
ME visible on:
- Geophones only
~90 cm
MicrOBS
ME visible on:
- Hydrophone for very strong events
- Geophones
~30 cm
ARMSS
ME visible on:
- Hydrophone
- Geophones
0 - 5 cm

Figure 2

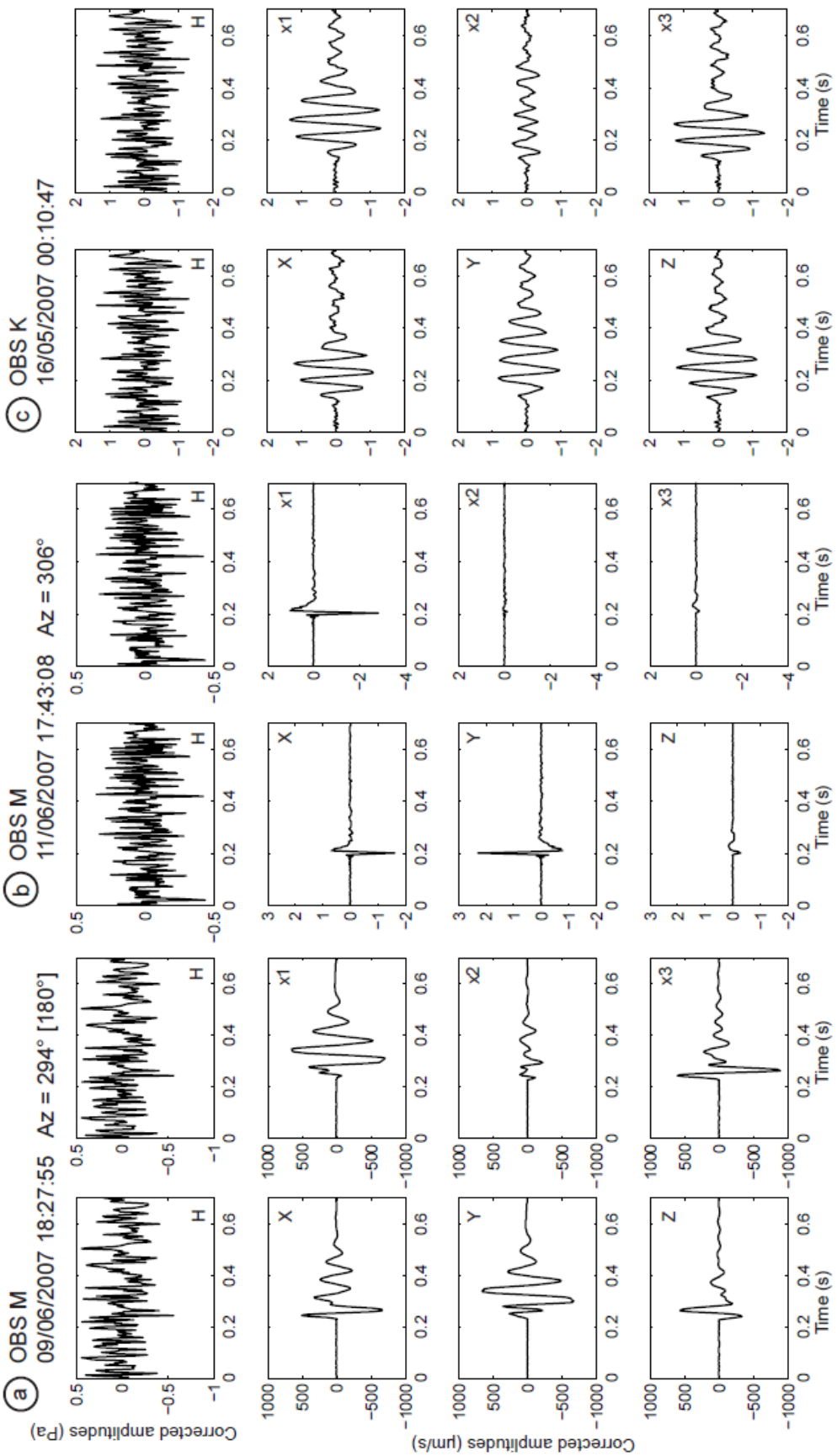
a OBS M
09/06/2007 18:27:55 Az = 294° [180°]
b OBS M
11/06/2007 17:43:08 Az = 306°
c OBS K
16/05/2007 00:10:47
H
X
Y
Z
x1
x2
x3
Time (s)
Corrected amplitudes (Pa)
Corrected amplitudes (μm/s)

Figure 3

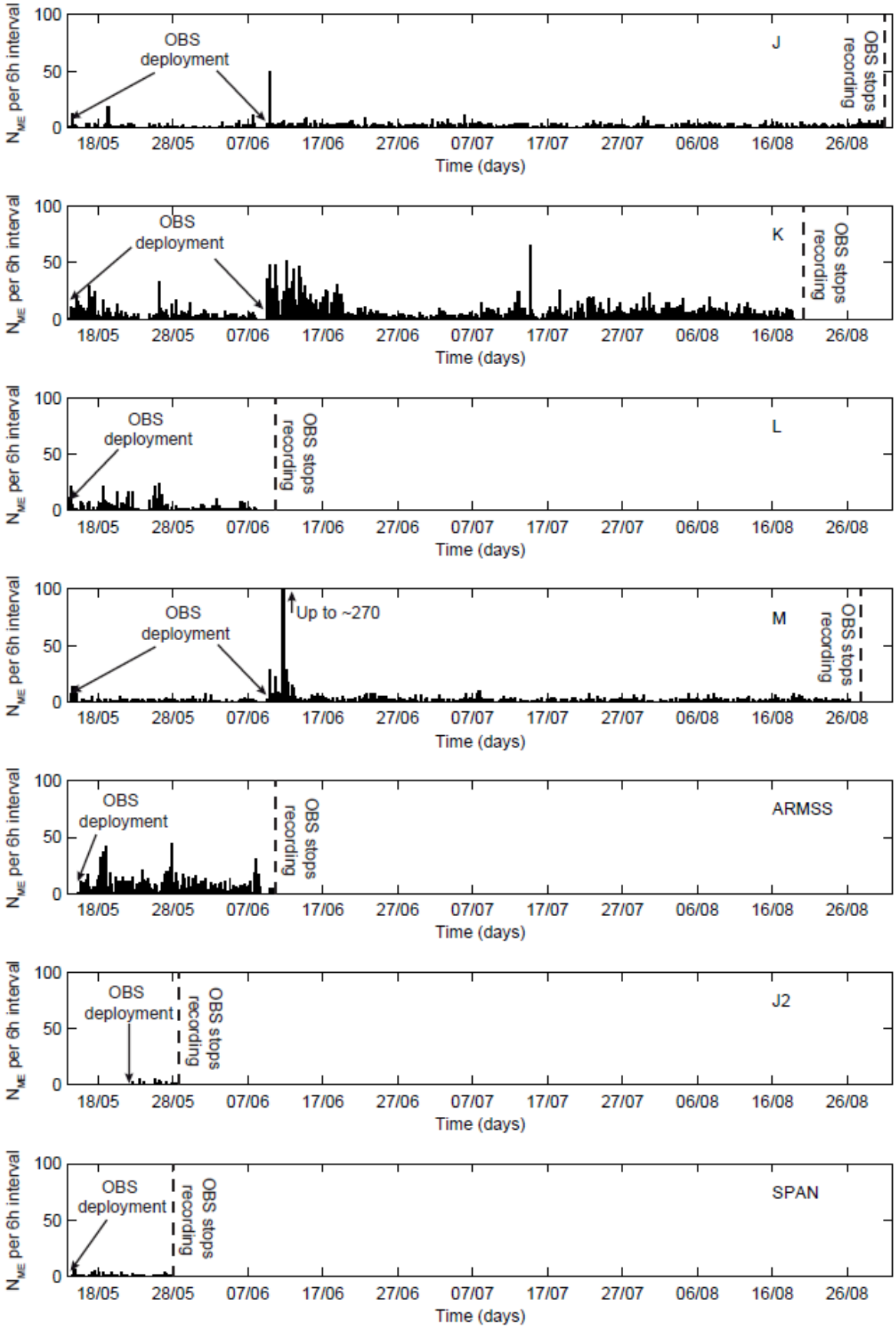
N_ME per 6h interval
100
50
0
OBS deployment
OBS stops recording
J
K
L
M
ARMSS
J2
SPAN
Up to ~270
18/05
28/05
07/06
17/06
27/06
07/07
17/07
27/07
06/08
16/08
26/08
Time (days)

Figure 4

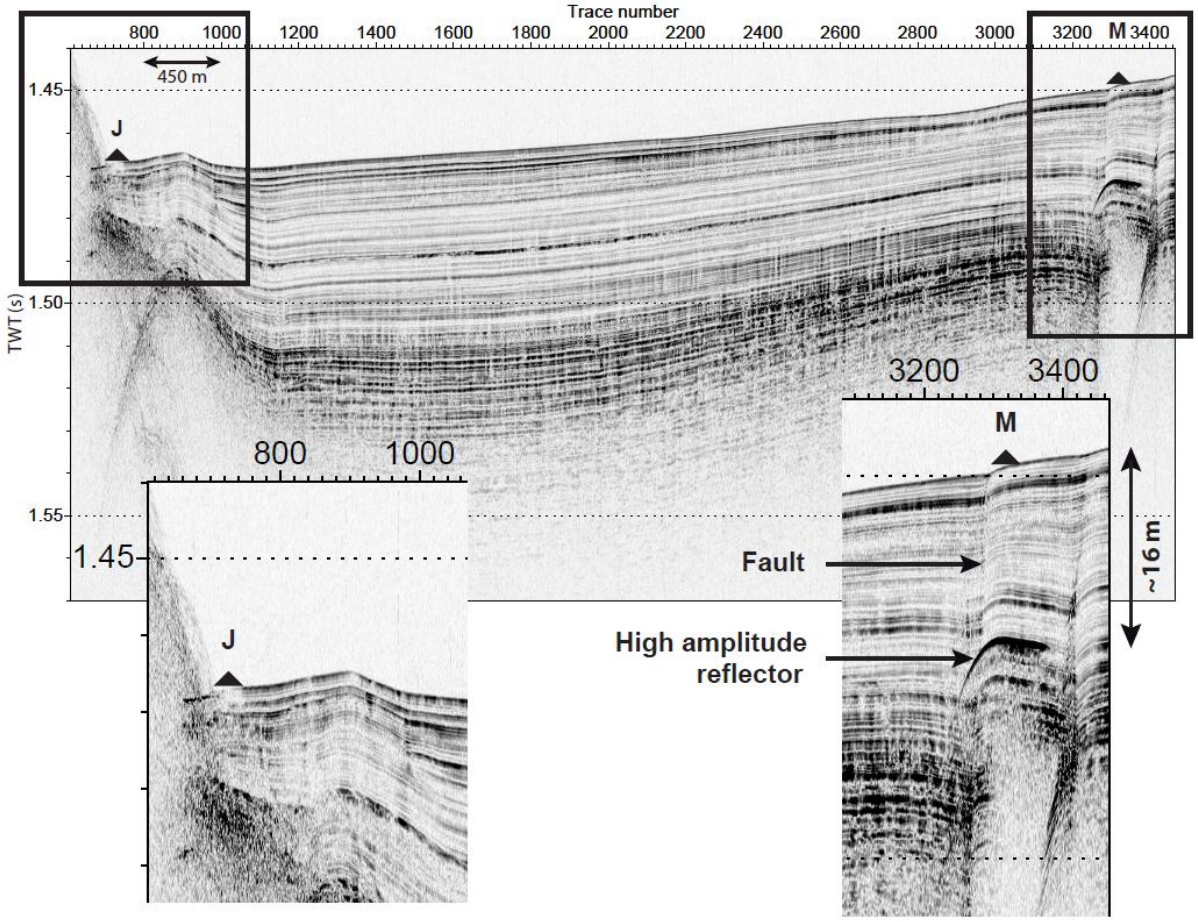
Trace number
800
1000
1200
1400
1600
1800
2000
2200
2400
2600
2800
3000
3200
M
3400
450 m
1.45
J
1.50
TWT (s)
1.55
3200
3400
M
800
1000
1.45
J
Fault
High amplitude
reflector
~16 m

Figure 5

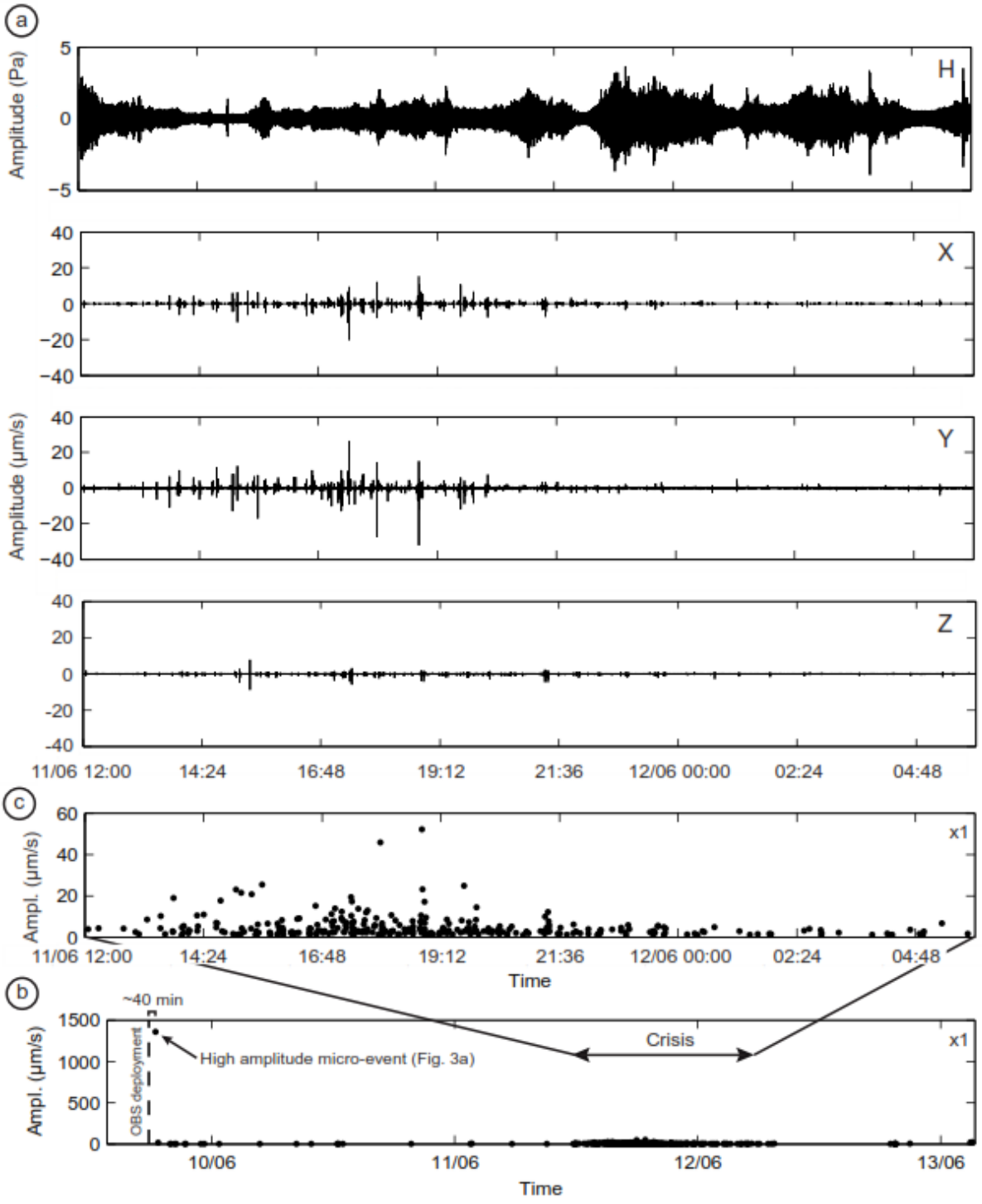
a
Amplitude (Pa)
H
X
Amplitude (µm/s)
Y
Z
11/06 12:00
14:24
16:48
19:12
21:36
12/06 00:00
02:24
04:48
c
Ampl. (µm/s)
x1
Time
b
~40 min
OBS deployment
High amplitude micro-event (Fig. 3a)
Crisis
10/06
11/06
12/06
13/06

Figure 6

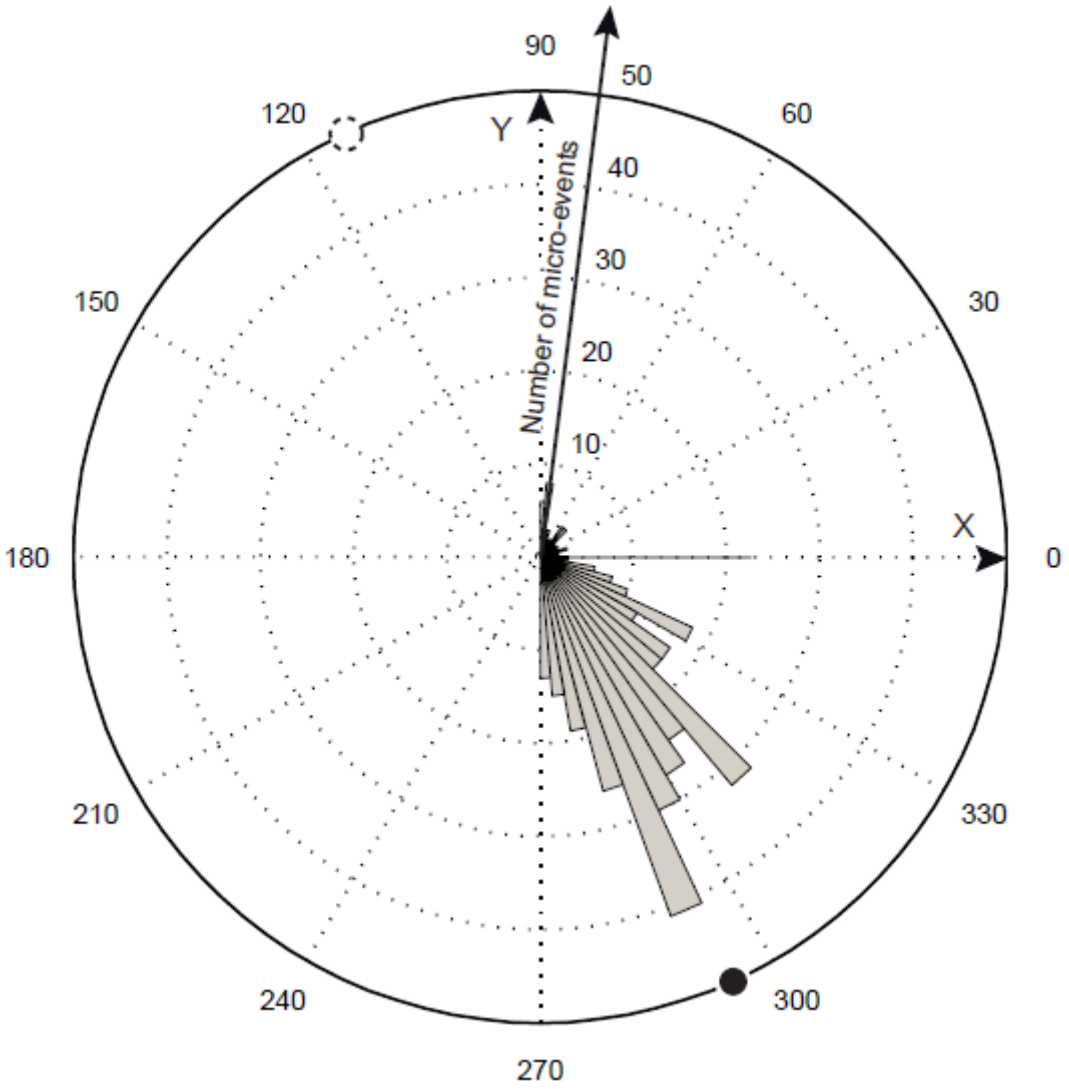
90
50
120
60
Y
40
30
150
30
Number of micro-events
20
10
X
180
0
210
330
240
300
270

Figure 7

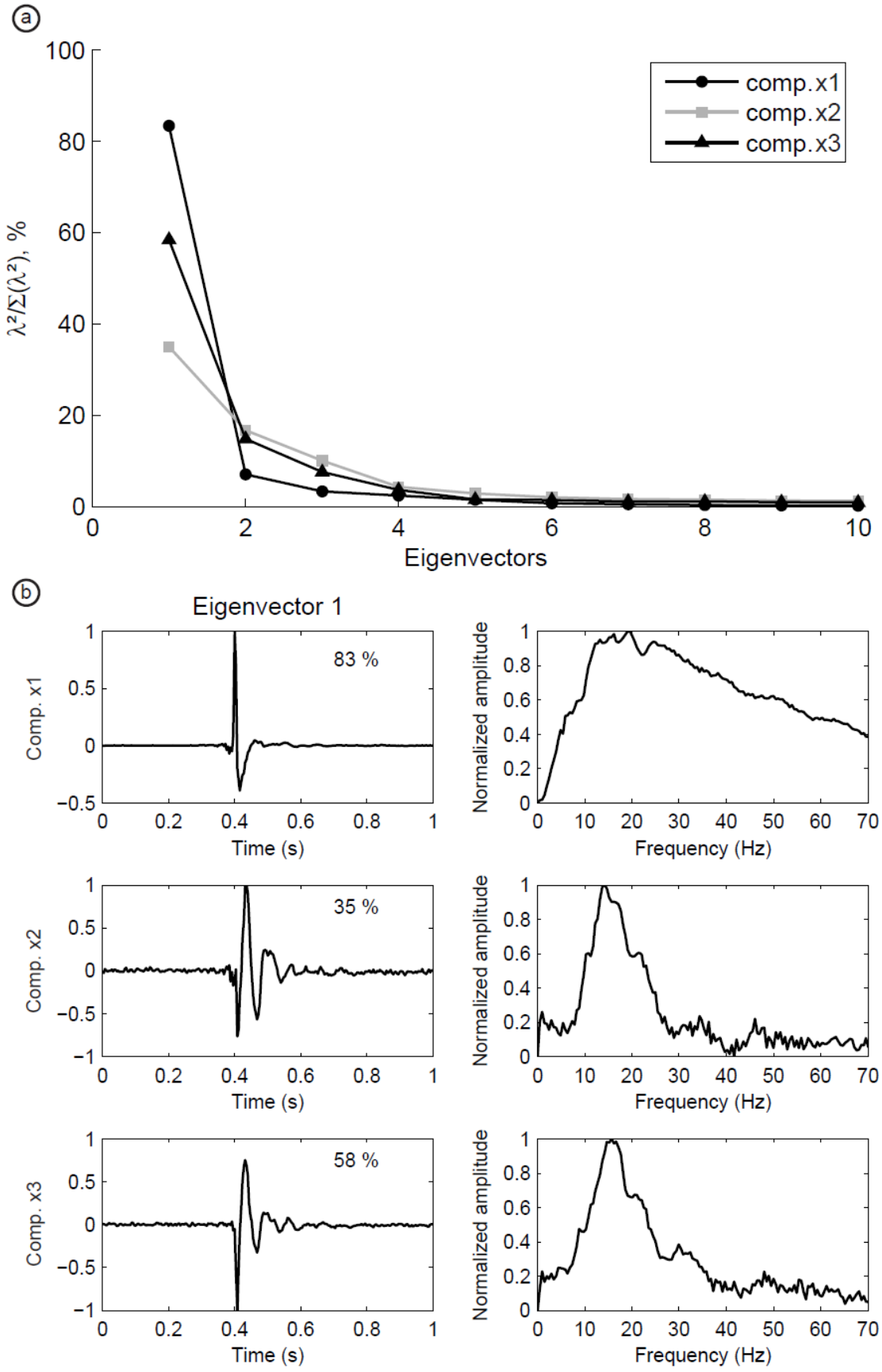
a
100
80
60
40
20
0
λ²/Σ(λ²), %
0
2
4
6
8
10
Eigenvectors
comp.x1
comp.x2
comp.x3
b
Eigenvector 1
Comp. x1
83 %
Comp. x2
35 %
Comp. x3
58 %
Time (s)
Normalized amplitude
Frequency (Hz)

Figure 8

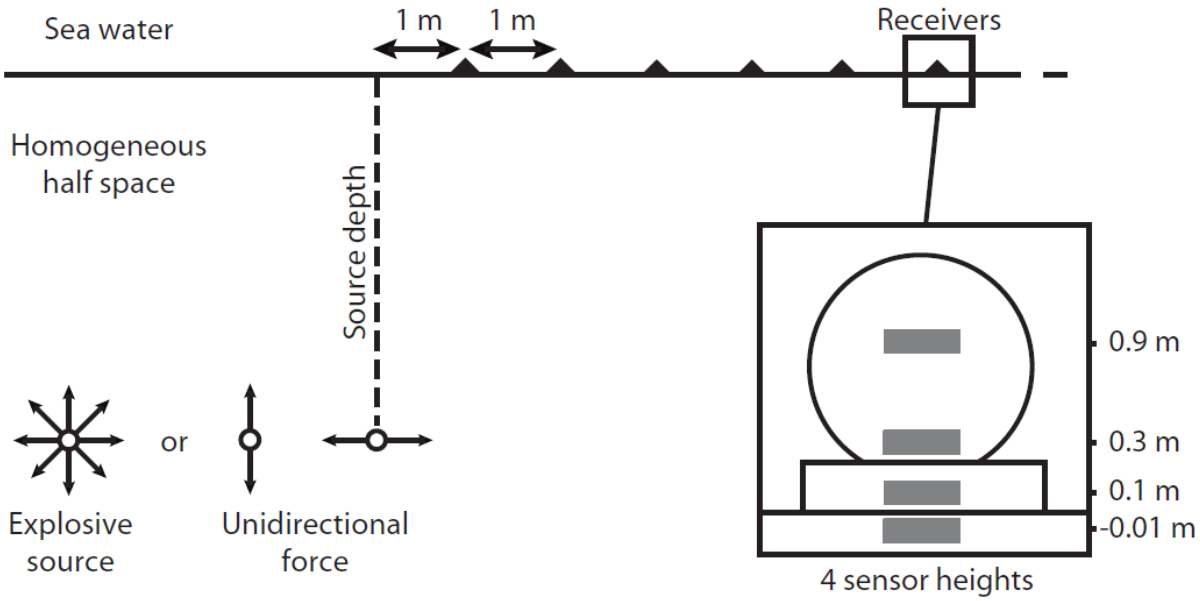
Sea water
1 m
1 m
Receivers
Homogeneous
half space
Source depth
0.9 m
0.3 m
0.1 m
-0.01 m
or
Explosive
source
Unidirectional
force
4 sensor heights

Figure 9

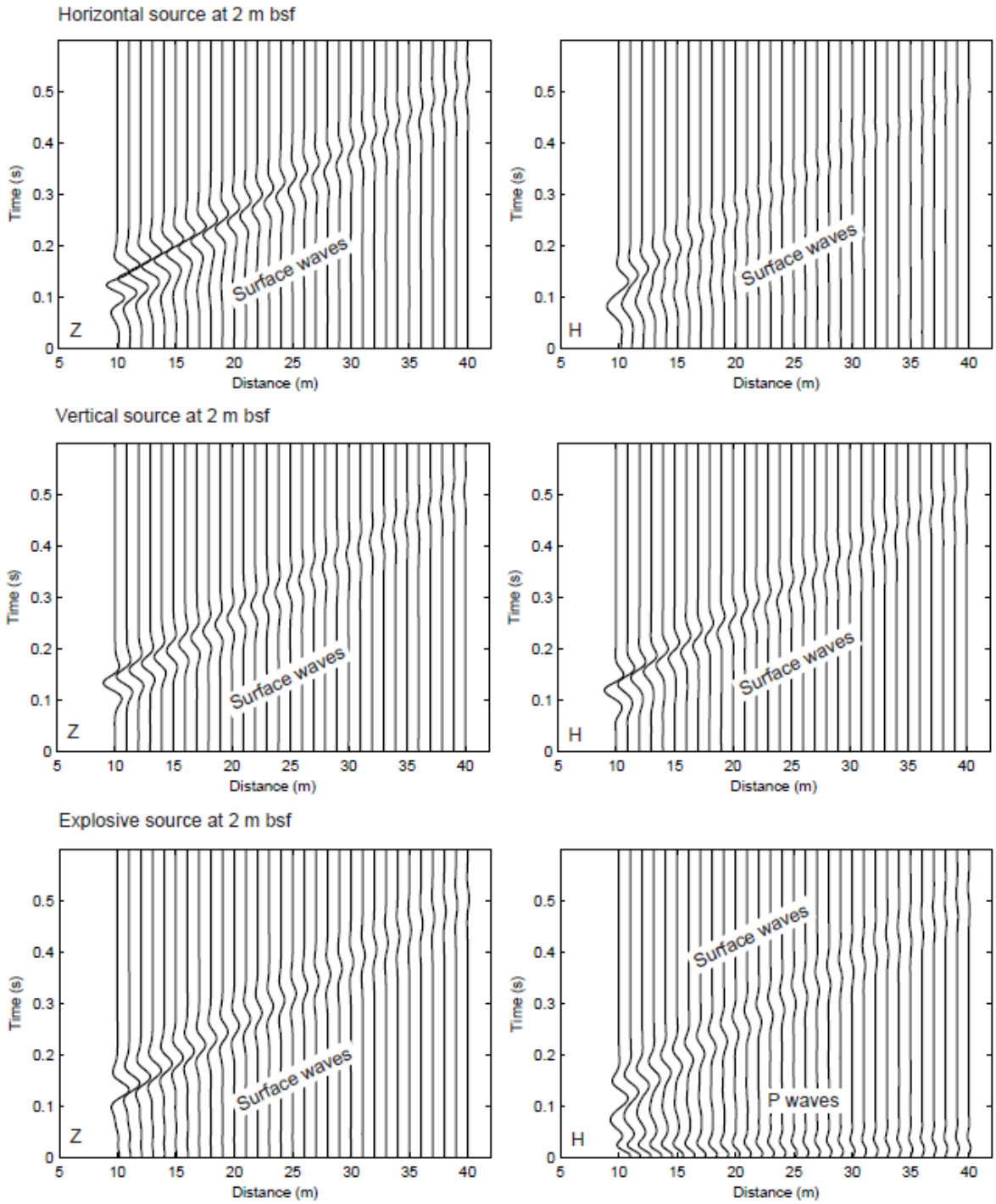
Horizontal source at 2 m bsf
Vertical source at 2 m bsf
Explosive source at 2 m bsf
Time (s)
Distance (m)
Surface waves
P waves
Z
H

Figure 10

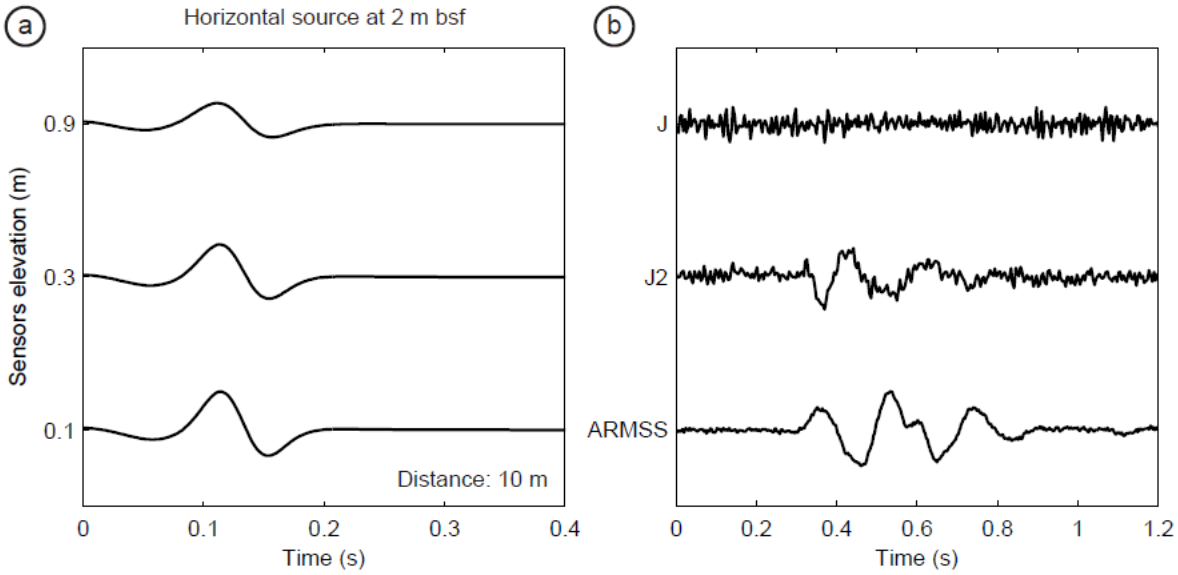
a
Horizontal source at 2 m bsf
Sensors elevation (m)
0.9
0.3
0.1
Distance: 10 m
0
0.1
0.2
0.3
0.4
Time (s)
b
J
J2
ARMSS
0
0.2
0.4
0.6
0.8
1
1.2
Time (s)

Figure 11

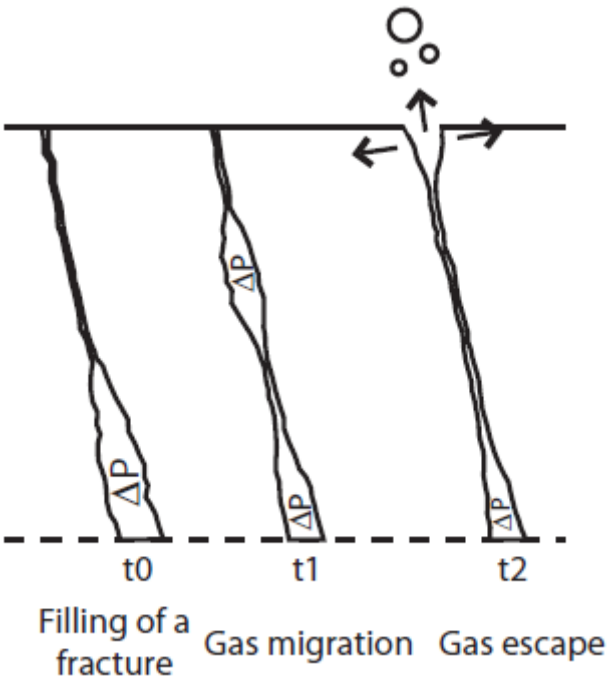
ΔP
ΔP
ΔP
t0
t1
t2
Filling of a fracture
Gas migration
Gas escape

Figure 12